MATERIALS SCIENCE

Highly stable and active catalyst in fuel cells through surface atomic ordering

Yanling Ma[1], Jiaheng Peng[1], Jiakang Tian[1], Wenpei Gao[1,2,3,4]*, Jialiang Xu[5], Fan Li[1], Peter Tieu[6], Hao Hu[1], Yi Wu[1], Wenlong Chen[1], Lei Pan[1], Wen Shang[1], Peng Tao[1], Chengyi Song[1], Hong Zhu[1], Xiaoqing Pan[2,7]*, Tao Deng[1,8]*, Jianbo Wu[1,4,8,9]*

Shape-controlled alloy nanoparticle catalysts have been shown to exhibit improved performance in the oxygen reduction reaction (ORR) in liquid half-cells. However, translating the success to catalyst layers in fuel cells faces challenges due to the more demanding operation conditions in membrane electrode assembly (MEA). Balancing durability and activity is crucial. Here, we developed a strategy that limits the atomic diffusion within surface layers, fostering the phase transition and shape retention during thermal treatment. This enables selective transformation of platinum-iron nanowire surfaces into intermetallic structures via atomic ordering at a low temperature. The catalysts exhibit enhanced MEA stability with 50% less Fe loss while maintaining high catalytic activity comparable to that in half-cells. Density functional calculations suggest that the ordered intermetallic surface stabilizes morphology against rapid corrosion and improves the ORR activity. The surface engineering through atomic ordering presents potential for practical application in fuel cells with shape-controlled Pt-based alloy catalysts.

INTRODUCTION

Proton exchange membrane fuel cells (PEMFCs) are promising energy conversion devices (*1*–*5*). However, the efficiency, power density, and practical lifetime of PEMFCs are adversely affected by the sluggish oxygen reduction reaction (ORR) at the cathode (*5*–*8*). This limitation causes the challenges in commercial Pt/C ORR catalysts, which include high cost, moderate activity, and degradation in long-term operation. To tackle the challenges, various platinum (Pt)–based nanomaterials have been developed (*9*, *10*). Shape-controlled alloy nanocrystals, in particular, show improved activities and stability in rotating disk electrode (RDE) tests; however, the harsh operation conditions in a fuel cell, including continuous potential fluctuations, elevated operating temperature, and high working current density, can lead to rapid leaching and degradation in membrane electrode assemblies (MEAs) (*5*, *11*–*19*). In addition, the leached metal cations in the MEA would accumulate near the surface and hinder proton transport (*20*). Therefore, enhancing the stability of shape-controlled Pt-based alloy ORR catalysts, as tested in the RDE, is vital for their efficient application in the cathodic layers of PEMFCs.

Considering that the ORR occurs on the surface of electrocatalysts, which is a heterogeneous interface between the liquid and solid, to improve the catalytic activity thus requires fine-tuning of the surface structure and the surface electronic states. On the surface, undercoordinated metal atomic sites are more active but susceptible to oxidation or corrosion. To enhance the stability of ORR catalysts is therefore pivotal for the practical use of fuel cells. Because structurally ordered intermetallic phases display corrosion resistance due to a more negative enthalpy, strong heteroatomic bonding, and atomistic uniformity in composition (*21*–*27*), transforming disordered surfaces of shape-controlled Pt-based alloy catalysts into intermetallic structures can promote long-term durability and maintain high ORR catalytic activity in MEAs (*28*–*30*).

Thermal annealing is a traditional method to create intermetallics in metallurgy, but mainly for spherical nanoparticles (NPs) (*31*–*33*), because the elevated temperatures applied to drive the disorder-to-order transformation often lead to surface reshaping and sintering (*34*–*36*), especially for shape-controlled nanocrystals, where the exposed surfaces are not thermodynamically stable, therefore resulting in the loss of optimized activity associated with the desired shape. Methods using mesoporous silica or silica protection to mitigate the nanostructure aggregation have been developed, where additional etching is required to remove the silica (*37*, *38*). For the direct synthesis of nanostructured catalysts with an intermetallic phase, the key is to initiate the disorder-to-order transformation and limit the process only at the surface layers (*22*, *39*). This requires precise control of the annealing process, enabling atomic diffusion only in the surface region while leaving the interior area unaffected to preserve the shape (fig. S1).

Here, we used in situ scanning transmission electron microscopy (STEM) to identify optimal conditions for preserving the shape while inducing disorder-to-order phase transition in one-dimensional (1D) PtFe nanowires (NWs), with a focus on quantifying the impact of annealing temperature and time on the deformation and ordering process. We found that surface atomic diffusion and ordering occurred at a notably low temperature, ~200°C lower than the typical phase transition temperature of the bulk (>550°C), for nanosized PtFe alloy. This low temperature suppressed atomic motion within the interior region of the NW, preventing the morphology change and sintering. On the basis of the finding, we successfully synthesized

[1]State Key Laboratory of Metal Matrix Composites, School of Materials Science and Engineering, Shanghai Jiao Tong University, 800 Dongchuan Road, Shanghai 200240, P. R. China. [2]Department of Materials Science and Engineering, University of California, Irvine, 5200 Engineering Hall, Irvine, CA 92697, USA. [3]Department of Materials Science and Engineering, North Carolina State University, 911 Partners Way, Raleigh, NC 27695, USA. [4]Future Material Innovation Center, Zhangjiang Institute for Advanced Study, Shanghai Jiao Tong University, Shanghai 200240, P. R. China. [5]University of Michigan-Shanghai Jiao Tong University Joint Institute, Shanghai Jiao Tong University, 800 Dongchuan Road, Shanghai 200240, P. R. China. [6]Department of Chemistry, University of California, Irvine, 1102 Natural Science II, Irvine, CA 92697, USA. [7]Department of Physics and Astronomy, University of California, Irvine, 4129 Frederick Reines Hall, Irvine, CA 92697, USA. [8]Center of Hydrogen Science, Shanghai Jiao Tong University, 800 Dongchuan Road, Shanghai 200240, P. R. China. [9]Materials Genome Initiative Center, Shanghai Jiao Tong University, 800 Dongchuan Road, Shanghai 200240, P. R. China.
*Corresponding author. Email: wgao9@ncsu.edu (W.G.); xiaoqing.pan@uci.edu (X.P.); dengtao@sjtu.edu.cn (T.D.); jianbowu@sjtu.edu.cn (J.W.)

surface intermetallic PtFe NW catalysts (Surf-IM-PtFe NWs) from PtFe alloy NWs at the gram scale. The much improved activity and stability observed in RDE measurements were well translated to the MEA performance (*5*, *11*, *12*). The mass activity (MA) at 0.9 $V_{iR\text{-}free}$ exceeded twice that of the PtFe NWs, retaining 78.6% of its initial value after 30k cycles in a H_2-O_2 fuel cell, surpassing the durability target (<40% MA loss) (*40*). At 80°C under acidic conditions, the Surf-IM-PtFe NWs show notably reduced Fe loss of 41.3%, compared with that of the randomly alloyed PtFe NWs (94.1% in loss) after the 30k cycle durability test. Density functional theory (DFT) calculations attribute the enhanced stability of Surf-IM-PtFe NWs to their corrosion-resistant intermetallic surface. This method to produce surface intermetallic nanostructures paves way to the design of stable shape-controlled Pt-based ORR catalysts with practical applications in fuel cells.

RESULTS

In situ growth of surface intermetallic PtFe NWs

The free-standing PtFe alloy NWs with a diameter of around 3 nm were synthesized in solid state using a generic method published previously (details in Materials and Methods and figs. S2 to S7) (*41*). Dangling atoms are visible on the edge of the pristine NWs and highlighted by yellow dashed circles (fig. S4B). The randomly alloyed structure was confirmed by the fast Fourier transform (FFT) pattern displaying only the diffraction spots from the face-centered cubic (fcc) A1 phase and the x-ray energy-dispersive spectroscopy (EDS) elemental maps showing uniform Fe and Pt distribution (fig. S5B). To study the disorder-to-order transition process, the free-standing PtFe NWs were dispersed onto a thermal E-chip of the heating holder for in situ STEM imaging (*41*–*44*) during annealing from room temperature to high temperature, with a holding time of 30 min at every 50°C increment. The 1D morphology was preserved up to 350°C without any aggregation or breakage (fig. S8). In Fig. 1, a single PtFe NW was imaged along its [001] zone axis at 350°C. In the high-angle annular dark-field (HAADF)-STEM image, the periodic squared lattice of Fe columns with darker intensity and the Pt columns with brighter intensity are visible on the surface (Fig. 1A). Both the (100) and (010) diffraction spots from the ordered $L1_2$ phase of Pt_3Fe appear in the FFT pattern (Fig. 1B) from the surface region but absent in the as-synthesized PtFe NWs. This observation well fits the unit cell model of the intermetallic $L1_2$ structure, sketched in Fig. 1C, where Fe atoms occupy the eight corners and Pt the face centers. To further provide the details of the surface structure, a false-color image taken from the yellow box in Fig. 1A is magnified in Fig. 1D. The intensity profiles along two framed regions are shown in Fig. 1 (E and F), respectively. Within the green rectangle, atomic columns with periodic high and low intensity were picked from a to o, indicating the alternating Pt and Fe atoms. Vertically in the blue rectangle, the missing intensity oscillation after the atomic layer labeled as number 5 indicates that only the two exterior unit cells adopted the ordered Pt_3Fe phase. The cropped enlarged image in Fig. 1G taken from the red box in Fig. 1A corresponds well with the simulated HAADF-STEM image (Fig. 1H), which is obtained from a 3-nm-thick columnar atomic model of an ordered $L1_2$-Pt_3Fe NW, further confirming the formation of the intermetallic surface on PtFe NWs after low-temperature annealing. For a better understanding on the Surf-IM structure, fig. S9 demonstrates a simplified atomic model of the Surf-IM-PtFe NW with an ordered $L1_2$-Pt_3Fe shell and a randomly alloyed PtFe core.

Figure 2 (A to D) shows the sequential HAADF-STEM images of a selected NW during the structural evolution to determine the dynamics of the surface atomic ordering under low temperatures. In Fig. 2A, the near-surface region of the NW was in a disordered phase at 250°C, as indicated by the intensity of the atomic columns (Fig. 2E). At 350°C (Fig. 2B), the outermost unit cell along the atomic layer in the [010] direction (marked by a magenta rectangle) started to show alternating Pt (bright) and Fe (dark) atomic columns, in correspondence to the intensity profile in Fig. 2F. After 15 min at 350°C (Fig. 2C), nearly the entire surface of PtFe NWs transformed to the $L1_2$-Pt_3Fe phase with a thickness of three unit cells (Fig. 2G). The new ordered surface became more faceted, showing distinct terraces after 18 min (Fig. 2, D and H). The simulated HAADF-STEM images using atomic models in the boxed area in the false-color images validated the structure evolution. A similar transformation trend given by another NW was also captured as shown in fig. S10. Although the evolution details such as the timeline varied with the thickness of the NWs, the atomic ordering was also found to proceed from the surface (fig. S10, A, B, E, and F) along with the interior atomic migration, suggesting the softening of the atomic lattice during the phase transition under low-temperature thermal annealing (fig. S10, I, J, M, and N). As shown in Fig. 2I, when the temperature was below 350°C, the in situ FFT patterns only showed the diffraction spots from the disordered fcc phase, but then the (100) and (010) superlattice reflections emerged and became clearer with extended time at 350°C. However, with the annealing time of more than half an hour or at the temperature up to 500° and 600°C, the PtFe NWs started to break (fig. S11).

The growth mechanism of surface intermetallic PtFe NWs

Using in situ STEM observation, we determined optimal annealing conditions for preserving the shape while inducing surface atomic ordering in 1D PtFe NWs. The temperature was capped at 350°C, and the durations did not exceed half an hour at this temperature. This surface atomic ordering occurs at low temperatures in NWs because the thermodynamics and kinetics during the phase transition are different from their bulk phase. Size effects affect transition temperature (*45*, *46*) as smaller materials exhibit lower energy barriers, enabling atomic ordering at reduced temperatures (*47*). The thin NWs in this work with few nanometers in diameter can further lower the temperature required for phase transition. The atomic ordering is thermodynamically driven, where the phase transformation's driving force $\Delta G_{b\rightarrow a}$ (the Gibbs free energy difference between phase a and b; fig. S12) depends on the annealing temperature (*48*, *49*). However, initiating lattice reconstruction needs to overcome an extra energy barrier Δg due to the attraction between atoms (Fig. 2J). Surface atoms, due to higher thermal vibration, migrate more easily. The undercoordinated atoms and weak interatomic interactions near the surface could further lower Δg (*47*, *50*–*52*). Thus, for atomic ordering in nanomaterials, there is a distinct difference between the surface and the interior. A lower energy barrier on the surface region ($\Delta g_{surface}$) is expected to facilitate the surface atomic ordering and phase segregation (Fig. 2J).

Besides, considering the preferential nucleation at the surface, the time-temperature-transformation diagram of the surface region (surface TTT) can be located in a low-temperature zone and the timescale to complete the surface atomic ordering is smaller (Fig. 2K). Note that, although the thermodynamics under low temperatures allow the transformation at the surface, the migration of the phase

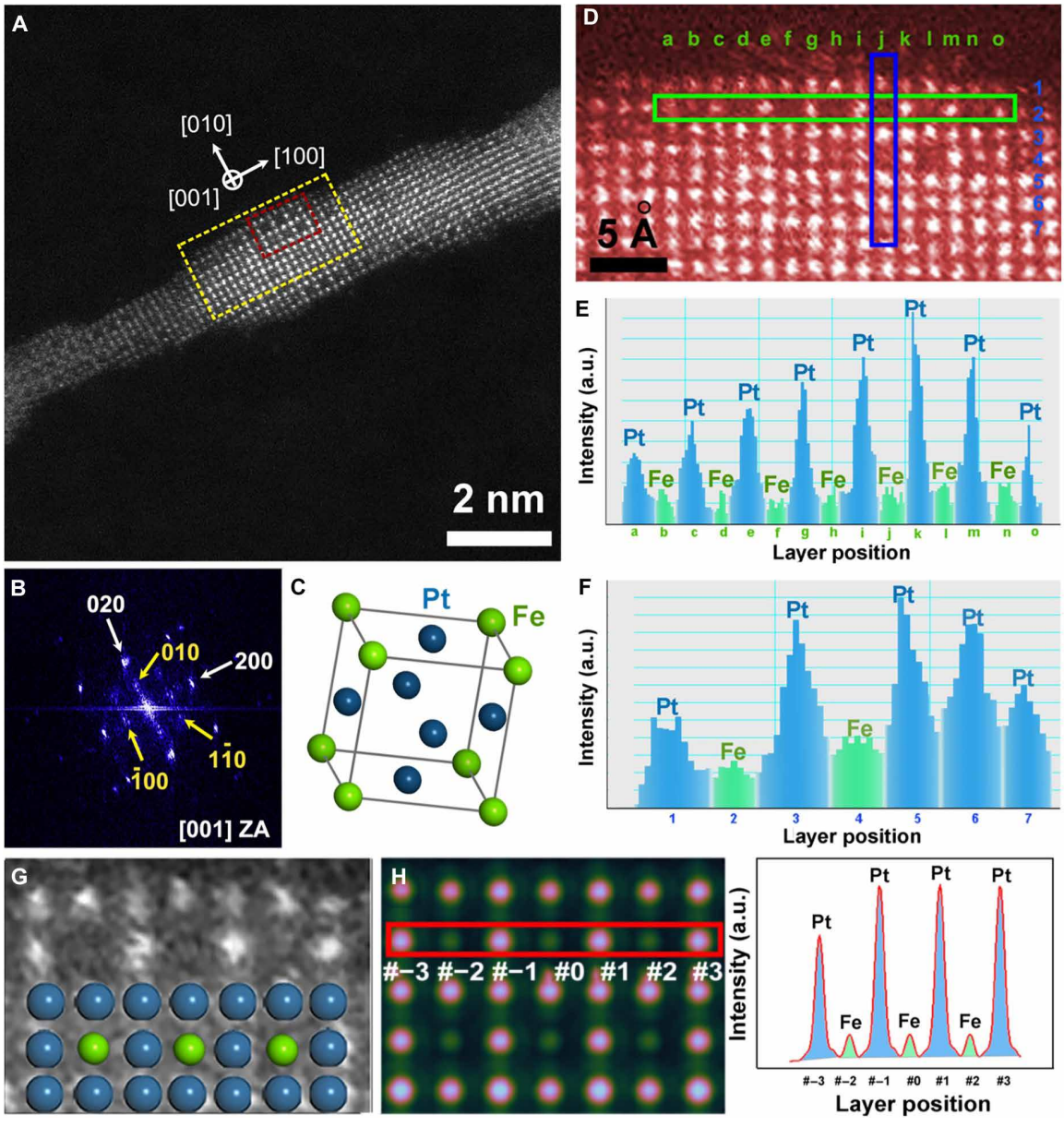

Fig. 1. Intermetallic surface formation on PtFe NWs under in situ low-temperature annealing. (**A**) HAADF-STEM image of the PtFe NW after being annealed at 350°C for 30 min. (**B**) Corresponding FFT pattern of the surface region in (A) with the superlattice spots from the disordered A1-PtFe phase (labeled by white arrows) and ordered $L1_2$-Pt_3Fe phase (labeled by yellow arrows). (**C**) Unit cell of the ordered $L1_2$-Pt_3Fe structure. Color code: Pt, blue; Fe, green. (**D**) Cropped false-color image from the yellow box in (A). (**E** and **F**) The corresponding intensity profiles along the atomic layers in (D) are circled by the green (E) and blue (F) rectangles, respectively. a.u., arbitrary units. (**G**) Cropped enlarged lattice from the red box in (A) and the corresponding atomic model. (**H**) Simulated HAADF-STEM image of the $L1_2$-Pt_3Fe model and the intensity profile from the atomic layer in the red rectangle.

boundary between the newly formed intermetallic phase and the randomly alloyed phase would be impeded due to the sluggish atomic diffusion in the interior of the NWs. The kinetics of the phase transformation then slow down greatly after stepping into the internal space. Accordingly, an ordered phase was only observed within the thickness of no more than three unit cells on the PtFe NWs after annealing at 350°C for 30 min. In this study, the overall atomic ratio between Pt and Fe is close to 1, but the ordered Pt_3Fe $L1_2$ phase formed rather than the PtFe $L1_0$ phase. It is because the surface segregation of Pt atoms and the lattice ordering induced by atomic diffusion happen simultaneously (*53*). During this process, the Fe atoms migrate out from the PtFe NW in air, as seen in the EDS mapping in fig. S5. Note that the surface atomic ordering is not driven by the compositional segregation because the disorder-to-order phase transition temperature is much higher (1300° to 1350°C for bulk PtFe and >550°C for PtFe nanomaterials) than the temperature we used (350°C). Therefore, this low-temperature surface atomic ordering (LT-SAO) approach might also be promising to transform the randomly alloyed surface into the ordered intermetallic structure and also retain the well-defined morphology of other Pt-based alloy nanocrystals.

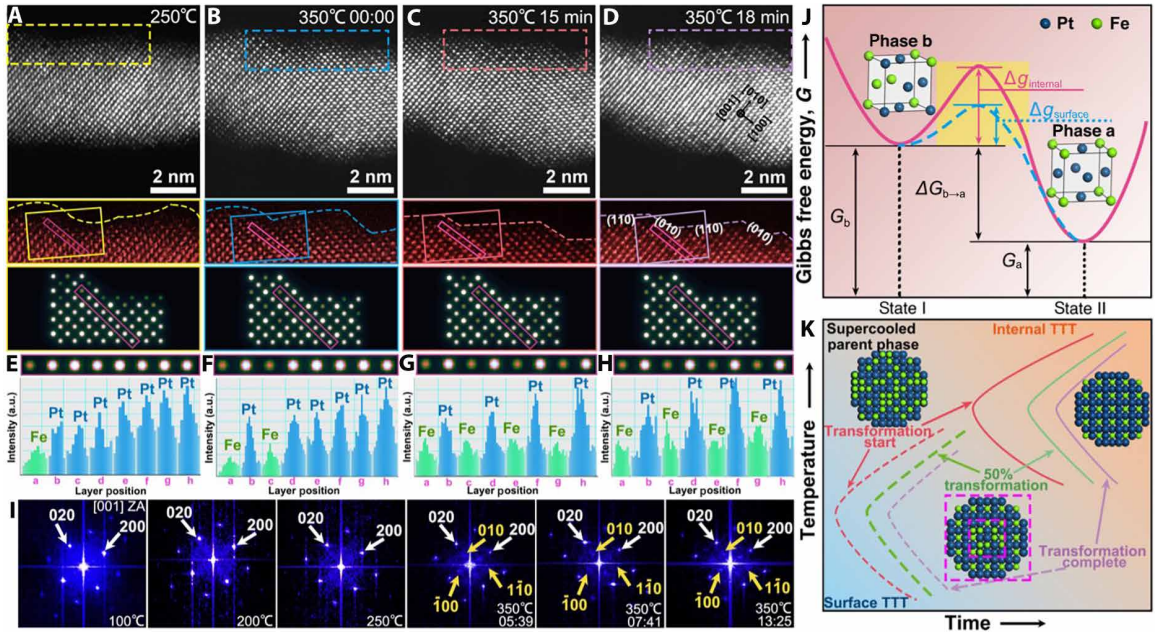

Fig. 2. Disorder-to-order transformation of the PtFe NW surface structure. (**A** to **D**) Sequential HAADF-STEM images taken along at 250°C, 350°C for 0 min, 350°C for 15 min, and 350°C for 18 min. Each enlarged false-color image corresponds to the near-surface region marked by a yellow, blue, pink, or purple dashed line box in (A) to (D), respectively. Each simulated HAADF-STEM image is obtained from the corresponding atomic model of the boxed area in the false-color image. (**E** to **H**) Intensity profiles along the atomic layers in the magenta rectangle of each false-color image. The labeled layer position of the *x* axis is counted downwards from the top. Each figure above is the zoom-in image of the atomic layer in the magenta rectangle in the simulated HAADF-STEM image, which also well fits with the intensity profiles. (**I**) Corresponding FFT patterns of the surface region under different temperatures or after different annealing times at 350°C. The FFT spots from the disordered fcc structure are labeled by white arrows, and the ones from the ordered $L1_2$-Pt_3Fe phase are labeled by yellow arrows. (**J**) Schematic illustration of the energy barrier $\Delta g_{internal}$ and $\Delta g_{surface}$ to transform from phase b to phase a. (**K**) TTT diagrams of surface and internal regions showing the kinetics of phase transformation from the supercooled parent phase to the ordered phase.

The electrocatalytic activity and durability evaluations during the ORR in MEAs

The reported PtFe-based electrocatalysts with randomly alloyed structures have demonstrated efficient ORR performance in liquid half-cells but are also prone to suffer severe degradation because Fe suffers more from galvanic corrosion than other non-noble transition metals (Cu, Co, Ni, etc.) in an acid electrolyte (*31*, *54*–*57*). Meanwhile, the abundant high-index facets on the 1D nanostructures that promote the fast ORR may also undergo preferential surface corrosion. Such characteristics make PtFe NWs perfect candidates to verify if the intermetallic surface is effective to improve the durability and maintain the controlled shape for high activity of ORR electrocatalysts in MEAs. To do so, we performed thermal annealing for the carbon-supported PtFe alloy NWs (denoted as PtFe NWs/C) in a tube furnace following the in situ LT-SAO protocols. Similarly, as the in situ results show, the breakage and aggregation occurred to the carbon-supported NWs at higher temperatures of 500° and 600°C (fig. S13), whereas the 1D morphology was well preserved both before and after the low-temperature treatment at 350°C (fig. S14). The dangling atoms were seen on the edge of the NWs before annealing (fig. S15A), similar to those in fig. S4B. After thermal annealing, the surface of NWs became smoother (fig. S15B) due to the surface atomic diffusion at the increased temperature (350°C). The clearer difference in the surface atomic structure before and after the low-temperature annealing could be seen from the HAADF-STEM images in Fig. 3A. The randomly arranged Pt and Fe atoms in the as-synthesized PtFe NWs became ordered in the surface region after the annealing, as indicated by the obvious periodic square array and the corresponding intensity profiles taken along the second near-surface atomic layer (fig. S16). In the x-ray diffraction (XRD) patterns (Fig. 3B), the broad peak around 25° corresponds to the carbon support. There were no peaks of (100) and (110) planes from the intermetallic $L1_2$-Pt_3Fe phase that emerged in the XRD pattern of the Surf-IM-PtFe NWs/C, except for a slightly positive shift when compared with the referenced commercial Pt/C and PtFe NWs/C, as shown in the enlarged region of the (220) peak, indicating that the NWs did not transform to a fully ordered intermetallic phase.

The ORR performance of the PtFe NW catalysts was first evaluated in a liquid half-cell using the RDE technique. The long-term stability was measured by conducting an accelerated durability test (ADT) of 30k cyclic voltammetry (CV) cycles in a 0.1 M perchloric acid ($HClO_4$) electrolyte. Figure 3C exhibits the comparison of the ORR polarization curves in which the commercial Pt/C and PtFe NWs/C delivered a negative shift of 45 and 199 mV, respectively, for the half-wave potential after the ADT. For the Surf-IM-PtFe NWs/C, it only demonstrated a loss of 3 mV, indicating the impressively enhanced stability. The electrochemical active surface area (ECSA) toward each catalyst was calculated from the stable CV curves shown in fig. S17. PtFe NWs/C, Surf-IM-PtFe NWs/C, and PtFe NWs/C-500-30 min obtained similar ECSAs, which were lower than that of commercial Pt/C as a result of the higher specific surface area given by 0D Pt NPs than 1D NWs (Fig. 3D). The normalized ORR catalytic activities were compared in Fig. 3 (E and F). At 0.9 V versus reference hydrogen electrode (RHE), Surf-IM-PtFe NWs/C delivered an MA of

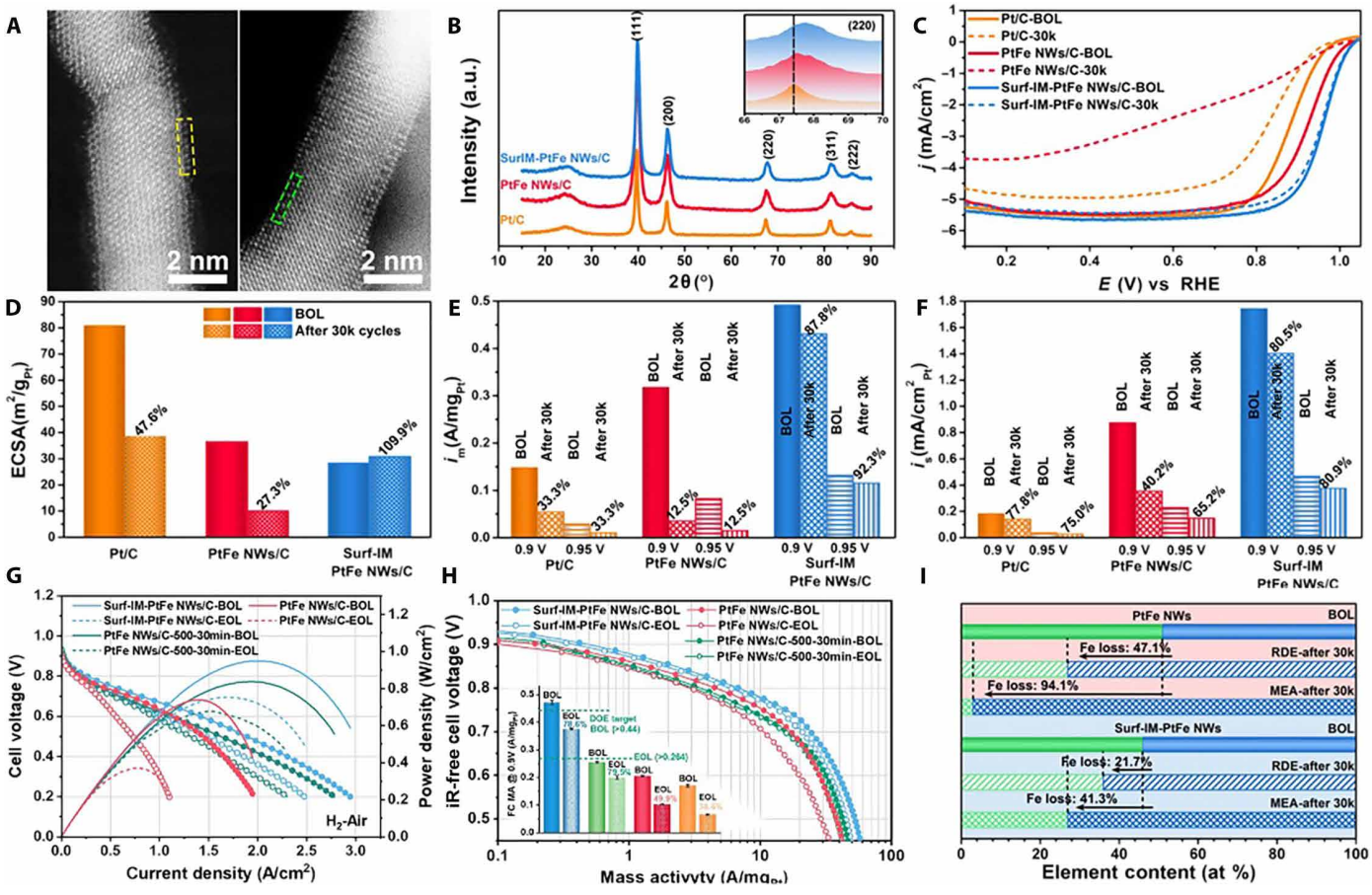

Fig. 3. Electrocatalytic activity and durability evaluations in a liquid half-cell and single fuel cell. (**A**) Atomic-resolution HAADF-STEM images of PtFe NWs/C (left) and Surf-IM-PtFe NWs/C (right). (**B**) XRD patterns of Pt/C, PtFe NWs/C, and Surf-IM-PtFe NWs/C. The inset shows the enlarged region of (220) diffraction peaks. (**C**) ORR polarization curves and (**D**) ECSA of Pt/C, PtFe NWs/C, and Surf-IM-PtFe NWs/C measured in a liquid half-cell before and after the ADT of 30k CV cycles. (**E** and **F**) Comparison of the MA and specific activity obtained from RDE measurements at 0.9 and 0.95 V before and after the ADT. BOL, beginning of life. (**G**) *i-V* polarization curves (symbols with lines) and power density plots (lines) of PtFe NWs/C and Surf-IM-PtFe NWs/C before (solid symbols with lines and solid lines) and after (hollow symbols with lines and dashed lines) the AST of 30k cycles in a H_2-air fuel cell with a cathode Pt loading of 0.1 mg_{Pt}/cm^2 at 80°C under 250-kPa H_2/air (100% RH). (**H**) Cathodic MA Tafel plots derived from the H_2-O_2 MEA measurement at 80°C under 150-kPa H_2/O_2 (100% RH) before (solid symbols with lines) and after (hollow symbols with lines) the AST of 30k cycles. The inset shows the corresponding fuel cell MA at 0.9 $V_{iR\text{-}free}$. (**I**) Element content of Pt and Fe in the evaluated catalysts before and after the AST in the fuel cell. at %, atomic %. Color code for the MEA performance in (G) and (H): red, PtFe NWs; blue, Surf-IM-PtFe NWs.

0.49 A/mg_{Pt} and a specific activity of 1.74 mA/cm^2_{Pt} at the beginning of life, which outperformed those of both PtFe NWs/C and commercial Pt/C. After an ADT of 30k cycles at room temperature, the commercial Pt/C exhibited a 77% loss of MA at both 0.9 and 0.95 V. The ORR activity of PtFe NWs/C decreased even more quickly as indicated by the loss of ECSA and the negative shift of the linear sweep voltammetry curves with increasing ADT sweep cycles. A severe loss of 87.5% in MA and 59.8% in specific activity at 0.9 V was observed, showing the poor durability of the as-synthesized PtFe alloy NWs during long-term operation. However, the Surf-IM-PtFe NWs/C catalysts displayed a marked stability with only 12.2% decrease in MA and 19.5% loss of specific activity at 0.9 V and 7.7% decrease in MA and 19.1% loss of specific activity at 0.95 V. PtFe NWs/C-500-30 min exhibited a lower MA (0.34 A/mg_{Pt}) and SA (1.11 mA/cm^2_{Pt}) due to the breakage and aggregation that occurred during heat treatment at 500°C for 30 min. Benefiting from the advantage of the intermetallic structure, PtFe NWs/C-500-30 min also exhibits superior stability with only 7.5% decrease in MA and 17.1% loss of SA at 0.9 V, and a negligible decrease in MA and 9.5% loss of SA at 0.95 V benefited from the intermetallic structure (fig. S17 and table S2).

We further evaluated the PtFe-based NWs and commercial Pt/C in a H_2-O_2 and H_2-air single fuel cell at 80°C by incorporating the catalysts into the cathode of the MEA. Figure 3G and fig. S18A show their *i-V* polarization curves and power density plots recorded under 250-kPa air with 100% relative humidity (RH) before and after the accelerated stress test (AST). The MEA with Surf-IM-PtFe NWs/C as cathodic catalysts exhibited both higher current density and peak power density (0.95 W/cm^2) than the one with the same loading of PtFe NWs/C (0.74 W/cm^2), PtFe NWs/C-500-30 min (0.83 W/cm^2), and commercial Pt/C (0.82 W/cm^2) in the entire polarization voltage region. The cathodic MA Tafel plots derived from the internal resistance–free (iR-free) *i-V* polarization curves recorded under 150-kPa O_2 with 100% RH are presented in Fig. 3H and fig. S18B. For reference, the *i-V* polarization curves and power density plots without iR-free recorded under 150-kPa O_2 with 100% RH were provided in figs. S18C and S19. The above peak power density values of the

H_2-air and H_2-O_2 fuel cell were presented as a histogram in fig. 20 (A and B), respectively. The higher activities and better stability of Surf-IM-PtFe NWs/C in a liquid half-cell well translated into a comparable MEA performance. The fuel cell MA measured at 0.9 $V_{iR\text{-}free}$ is 0.47 A/mg_{Pt}, which achieved the 2025 activity target of 0.44 A/mg_{Pt}. Besides, it only represented a loss of 21.4% after conducting the AST, which also exceeded the durability target of <40% MA loss (*40*). The fuel cell assembled with PtFe NWs/C-500-30 min exhibits a lower MA (0.25 A/mg_{Pt}) measured at 0.9 $V_{iR\text{-}free}$ (Fig. 3H and the corresponding inset) due to some breakage and agglomeration of NW structures (fig. S13A), but it only represented a loss of 20.5% after conducting the AST that benefited from the intermetallic structure. In addition, the fuel cell assembled with PtFe NWs/C and commercial Pt/C both exhibit the lower MA (0.20 and 0.17 A/mg_{Pt}) and the larger loss of 50.1 and 61.4% after the AST, respectively. The above values of MA are recorded in the inset of Fig. 3H. For comparison, the performance of state-of-the-art PtFe-based and Pt-based random alloy catalysts evaluated in the RDE and MEA are provided in fig. S21 and table S4. The Surf-IM-PtFe NWs/C demonstrated a superior MA retention at the end of life (EOL) after 30k cycles, especially in a single fuel cell. Moreover, it is worth noting that the catalytic ORR activity obtained in MEAs is quite close to that from the RDE, which has never been reported in the published works.

To understand the structural and compositional stability of the catalysts, the samples on the glassy carbon electrodes and the cathode catalyst layer of the MEA were collected after the ADT or AST for each measurement. The quantitative TEM-EDS analysis shows that the rapid leaching of Fe occurred to the PtFe NWs after 30k cycles with a loss of 47.1% in a half-cell and an even higher loss of 94.1% in a fuel cell. In contrast, the Surf-IM-PtFe NWs demonstrated greatly suppressed corrosion toward Fe with the loss of less than half of that for PtFe NWs at the EOL (Fig. 3I and figs. S22 to S24). The HAADF-STEM image in fig. S22 further confirmed that the intermetallic surface of the Surf-IM-PtFe NWs still remained after the ADT in an acid. Therefore, the LT-SAO strategy proves to play a critical role in stabilizing the 1D NW morphology and greatly inhibited the leaching rate of the non-noble transition metal in the Pt-based alloy. The Surf-IM-PtFe NWs are shown to be a prominent candidate as a highly stable ORR electrocatalyst for PEMFCs.

Improving the catalyst stability through surface ordering

The activity degradation of PtFe ORR electrocatalysts can be ascribed to the inevitable dissolution of Fe under galvanic corrosion in an acid electrolyte. However, the corrosion potential of alloy can hardly be measured experimentally. To better understand the enhanced stability of the Surf-IM-PtFe NW catalysts, we conducted DFT calculations on the atomic models of two surface structures, including the ordered $L1_2$-Pt_3Fe phase and random A1-PtFe phase as shown in fig. S23. The calculated Pourbiax phase diagram provided by the Materials Project (*58*), which is plotted as functions of pH and the equilibrium potential using standard hydrogen electrode (SHE) as the reference, is illustrated in fig. S24. All the possible chemical equilibrium of the anodic oxidation reactions participated by the studied PtFe alloy are described as solid lines. The chemical equilibrium of the cathodic reduction reactions participated by oxygen or hydrogen during the galvanic corrosion is shown as the two red dashed lines in the phase diagram (inset in the bottom right corner of Fig. 4). Under an oxygen enrichment condition, when the pH is 1 and the ORR occurs with a reduction potential of 1.214 V versus SHE, PtO_2 and Fe^{3+} would be the stable oxidation products after the anode dissolution of both the ordered $L1_2$-Pt_3Fe phase and random A1-PtFe phase. Besides, the dissolution from Fe to Fe^{2+} can be regarded as the start of catalyst degradation. According to the calculations model for anodic dissolution developed based on thermodynamics and kinetics (details in Materials and Methods), the corresponding anode dissolution potentials of E(A1-PtFe|Pt, Fe^{2+}) and E($L1_2$-Pt_3Fe|Pt, Fe^{2+})E(Pt_3Fe|PtO_2, Fe^{3+}) were calculated to be −0.70 and −0.49 V, respectively, which indicates a preferential leaching out of Fe from the random A1-PtFe alloy rather than the ordered $L1_2$-Pt_3Fe. Furthermore, a considerably higher dissolution potential of 0.84 V for E($L1_2$-Pt_3Fe|PtO_2, Fe^{3+}) than that of 0.63 V for E(A1-PtFe|PtO_2, Fe^{3+}) suggested the better corrosion resistance

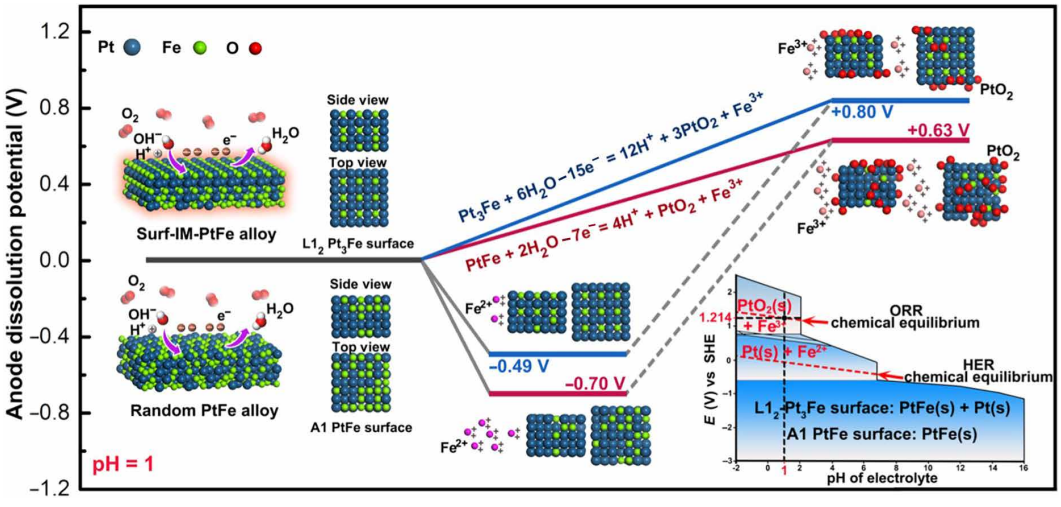

Fig. 4. Anode dissolution potential during galvanic corrosion. The galvanic corrosion process and the calculated anode dissolution potentials of two surface structures during the electrochemical cycling in an acid: ordered $L1_2$-Pt_3Fe phase (top) and random A1-PtFe phase (bottom). The inset shows a partial calculated Pourbiax phase diagram provided by the Materials Project. Phase regions are labeled by different color codes with the corresponding anodic dissolution products inside. HER, hydrogen evolution reaction.

of the structurally ordered $L1_2$-Pt_3Fe phase in the acidic environment. The poor electrochemical stability of the random A1-PtFe NW catalysts during the long-term operation, therefore, could be well explained. To further elucidate that the improved stability of the Surf-IM-PtFe NWs mainly originated from the effect of surface atomic ordering rather than the compositional change due to the surface segregation of Pt, we then calculated the dissolution potential of the random A1-Pt_3Fe alloy. It delivered a similar value as that of the ordered $L1_2$-Pt_3Fe phase with a formation enthalpy of 0.03 eV per atom, whereas the latter shows a much more negative value of −0.22 eV per atom. Such a difference could help greatly stabilize the structure, thus effectively inhibiting the corrosion (tables S5 to S7).

DFT calculations were also carried out to study the origin of the improved ORR activity of the Surf-IM-PtFe NW catalysts. The oxygen adsorption energy (ΔE_O) is widely accepted as the descriptor for ORR activities, which follows a simple correlation of the "volcano" plot. The optimal ΔE_O should be about 0.2 eV higher than that on the (111) surface of pure Pt (*6*, *59*, *60*). In this work, the most stable (111) surface was adopted to calculate the ΔE_O for each catalyst. Considering that the outermost Fe atoms could be etched away along with electrochemical cycling, all the adsorption slabs were built with a pure Pt layer on the top of the (111) surface. Because the O* prefers to adsorb on the hollow sites, all the possible hollow sites on the surface of the slabs were examined, and the most stable one was shown in fig. S25. For the Surf-IM-PtFe NWs, the structure with a one–unit cell–thick $L1_2$-Pt_3Fe intermetallic surface and the subjacent disordered PtFe alloy core was used for the simulation. It displayed a ΔE_O of −0.491 eV and a ΔE_O-ΔE_O^{Pt} of 0.494 eV, which potentially relieved the overbonding with O* species, indicating its favorable nature for ORR catalysis. However, for the PtFe alloy NWs, the calculated ΔE_O of −0.401 eV with a ΔE_O-ΔE_O^{Pt} of 0.584 eV showed much weaker adsorption toward the O* species, which would not help stabilize the OOH* species on the catalyst surface before O_2 activation (fig. S26).

DISCUSSION

For shape-controlled Pt-based alloy ORR catalysts, to bridge the gap between its high activity in RDE tests and the critical efficiency as cathodic catalyst layers in PEMFCs, it requires further improvements in the catalysts' long-term stability without loss in the catalytic activity. In this work, we propose a design concept of "surface intermetallics" and developed an LT-SAO strategy to achieve the surface disorder-to-order transition of 1D PtFe NWs with excellent ability for shape preservation. The thermodynamically favorable temperatures and optimal annealing time that drive the surface atomic ordering and simultaneously inhibit the global atomic diffusion were explored and identified using an in situ STEM study at atomic resolution. The high catalytic activities of the Surf-IM-PtFe NW catalyst evaluated by the RDE measurements were well translated into a comparable MEA performance, which has never been reported before. Compared with the completely random PtFe alloy NWs, the Surf-IM-PtFe NWs demonstrated a large enhancement in durability during the long-term operation in both the liquid half-cell and the H_2-O_2 single fuel cell. The catalyst also offers the state-of-the-art performance among all the PtFe-based and Pt-based alloy catalysts in MA retention with up to 78.6% of the pristine value after the AST in MEAs. DFT calculations further reveal that the formed intermetallic surface has a higher galvanic corrosion resistance that can substantially inhibit the rapid leaching out of Fe and effectively prevent the catalyst degradation. With these findings, the shape-controlled Surf-IM-Pt–based alloy nanocrystals prove to be a promising candidate for efficient cathodic ORR catalyst layers in PEMFCs. The design principle developed in this work would also pave the way for addressing the scientific and technological challenges at the catalyst level toward sustainable fuel cells.

MATERIALS AND METHODS

Chemicals and materials

Iron(II) chloride tetrahydrate ($FeCl_2{\cdot}4H_2O$, 98%) and potassium chloroplatinite (K_2PtCl_4, 98%) were obtained from Aladdin. Amorphous carbon (Vulcan XC-72R) from Cabot was used as support materials. Commercial Pt/C catalyst (HP 20 wt % Pt) was purchased from Alfa Aesar, and commercial Pt/C catalyst (HP 40 wt % Pt) was purchased from JM. Isopropanol (C_3H_8O, AR, ≥99.7%), anhydrous ethanol (EtOH, AR, ≥99.7%), and methanol (CH_4O, AR, ≥99.7%) were purchased from Sinopharm Chemical Reagent Co. Ltd. Concentrated perchloric acid ($HClO_4$, 70%) was obtained from Sigma-Aldrich. Argon (Ar, 99.999%) and hydrogen (H_2, 99.999%) were supplied by Shanghai Weichuang Standard Gas Analytical Technology Co. Ltd.

Catalyst preparation

Synthesis of ultrathin free-standing PtFe alloy NWs

In the typical preparation of free-standing PtFe NWs, K_2PtCl_4 (83.02 mg) and $FeCl_2{\cdot}4H_2O$ (39.76 mg) were dissolved into deionized water (5 ml) and then sonicated for 10 s [Caution: The duration for sonication in this step should be as short as possible in the case of the oxidation of Fe(II). The color of the solution ought to be transparent orange red rather than reddish brown suspension]. The mixture was dried at 50°C in a vacuum oven and then placed into a quartz boat. Deionized water (20 μl) was then dropped onto the well-mixed blender, and the slurry-like reactant was immediately transferred into a tube furnace. The system was purged for 15 min using Ar (200 ml/min) and then switched to H_2/Ar (10/190 ml/min). The reduction of the precursors was performed at 250°C for 30 min (ramping rate of 10°C/min). After cooling down to room temperature, the system was purged using Ar before collecting the product. The samples were washed with deionized water and centrifuged twice at 6000 rpm for 5 min. The obtained free-standing PtFe NWs were stored in ethanol to prevent aggregation before any characterization.

To study the influence of iron precursors, a control experiment was carried out using the same synthetic method except that $FeCl_2{\cdot}4H_2O$ was replaced by $FeCl_3$.

Preparation of carbon-supported PtFe NW catalysts

A controlled amount of acid-treated amorphous carbon (Vulcan XC-72R) was dispersed in methanol and sonicated for 1 hour. The free-standing PtFe NWs stored in ethanol were transferred to the carbon black dispersion followed by additional sonication of 30 min. After being stirred overnight, the PtFe NWs/C catalyst was precipitated by centrifugation and dried at 50°C in a vacuum oven.

Surface engineering of PtFe NW catalysts

To obtain the surface intermetallics on PtFe NW catalysts, the as-prepared PtFe NWs/C catalysts were further annealed at 350°C for 30 min in a vacuum tube furnace (the setting temperature of the tube furnace was calibrated by a thermocouple to the actual

temperature of 350°C). The samples were denoted as Surf-IM-PtFe NWs/C.

Structural and compositional characterization

The low-magnification TEM images of the samples were taken by using a JEOL JEM-2100F microscope at an accelerating voltage of 200 kV. High-resolution TEM, HAADF-STEM, and EDS elemental mappings were conducted on a JEOL JEM-ARM200F microscope at an accelerating voltage of 200 kV and a JEOL Grand ARM CF300 microscope at an accelerating voltage of 300 kV. The powder XRD patterns were collected on a Shimadzu x-ray diffractometer (LabX XRD-6100) with Cu Kα radiation resource. The accurate metal loading on the RDE was determined by Inductively Coupled Plasma-Atomic Emission Spectroscopy (ICP-AES, iCAP6300 instrument) and thermogravimetric analysis using a Netzsch DSC404 instrument.

In situ STEM imaging

The in situ study was carried out on a JEOL Grand ARM CF300 microscope at the University of California, Irvine, using the Protochips Fusion heating holder. The microscope was operated under STEM imaging mode. The free-standing PtFe NWs were dispersed in methanol and casted onto the heating E-chip. The temperature was increased to each specific temperature with a ramping rate of 1°C/s in vacuum.

Electrocatalytic performance evaluation

Preparation of the catalyst ink

The carbon-supported catalysts (5 mg) were dispersed into a mixed solvent of deionized water (4 ml), isopropanol (1 ml), and 5% Nafion (25 μl). After sonication for 15 min, the catalyst ink of PtFe NWs/C, Surf-IM-PtFe NWs/C, and commercial Pt/C catalysts was dropped onto the RDE. The accurate loading of the catalysts was determined to be 20.4 $\mu g_{Pt}/cm^2$ for Pt/C, 29.1 $\mu g_{Pt}/cm^2$ for PtFe NWs/C, and 52.1 $\mu g_{Pt}/cm^2$ for Surf-IM-PtFe NWs/C.

Electrochemical performance measurement

The ORR performances of all the obtained catalysts were evaluated using a three-electrode system and the RDE technique. The system includes a working electrode (glassy carbon RDE with an area of 0.196 cm^2), a counter electrode (platinum filament with a diameter of 0.5 mm), and an RHE. The CV curves were recorded at room temperature in the electrolyte of an Ar-saturated $HClO_4$ solution (0.1 M). The potential scan range is from 0.05 to 1.0 V with a scan rate of 50 mV/s. The ORR performance test was conducted in the electrolyte of an O_2-saturated $HClO_4$ solution (0.1 M). The linear scan range was set from 0 to 1.1 V versus RHE with a scan rate of 10 mV/s. The ECSA was calculated based on the region of hydrogen species absorption (0.05 to 0.40 V) in the CV curves. The ADT was performed in the electrolyte of the Ar-saturated $HClO_4$ solution (0.1 M) between 0.6 and 1.0 V for 30k cycles. The potential scan rate was set to 100 mV/s. The ORR polarization curves were recorded both before and after the ADT.

MEA preparation and fuel cell test

The H_2-O_2 and H_2-air fuel cell performance was evaluated in a single cell using a commercial Scribner 850e fuel cell test system. The MEAs with an effective area of 6.25 cm^2 were prepared by the catalyst-coated membrane method. The obtained catalysts were incorporated into MEAs by ultrasonic spraying the well-dispersed catalyst ink onto the Nafion HP proton exchange membrane (GORE, 15 μm in thickness), and the commercial gas diffusion layer (Sigracet) was then pressed onto the two sides of a proton exchange membrane for 90 s under a pressure of 1 MPa. The MEAs were prepared with a Pt loading of 0.1 mg/cm^2 at the anode (commercial Pt/C, 40 wt % Pt, JM) and 0.1 mg/cm^2 at the cathode (PtFe NW-based catalysts and 40% Pt/C). The fuel cell was operated at 80°C, with 150-kPa H_2/O_2 and 250-kPa H_2/air (2/3 standard liter per minute (slm), 100% RH) for the anode and cathode, respectively. Before the performance testing, the single cells were activated continuously to obtain a stable condition.

The AST was conducted according to the US Department of Energy's AST protocol. Pure H_2 and N_2 were fed to the anode and cathode, respectively. The cell voltage was driven by an external potentiostat in a square sweep cycle between 0.6 and 0.95 V. Each voltage level was kept for 3 s.

Calculations

The DFT was conducted in the Vienna ab initio simulation package using the method of the projector augmented wave. The generalized gradient approximation formulation was used to describe the exchange and correlation functions with an energy cutoff of 400 eV using the Perdew-Burke-Ernzerhof.

Supplementary Materials

This PDF file includes:

Supplementary Text
Figs. S1 to S29
Tables S1 to S7
References

REFERENCES AND NOTES

1. M. K. Debe, Electrocatalyst approaches and challenges for automotive fuel cells. *Nature* **486**, 43–51 (2012).
2. J. Wu, H. Yang, Platinum-based oxygen reduction electrocatalysts. *Acc. Chem. Res.* **46**, 1848–1857 (2013).
3. M. Shao, Q. Chang, J. P. Dodelet, R. Chenitz, Recent advances in electrocatalysts for oxygen reduction reaction. *Chem. Rev.* **116**, 3594–3657 (2016).
4. Y.-J. Wang, W. Long, L. Wang, R. Yuan, A. Ignaszak, B. Fang, D. P. Wilkinson, Unlocking the door to highly active ORR catalysts for PEMFC applications: Polyhedron-engineered Pt-based nanocrystals. *Energy Environ. Sci.* **11**, 258–275 (2018).
5. K. Kodama, T. Nagai, A. Kuwaki, R. Jinnouchi, Y. Morimoto, Challenges in applying highly active Pt-based nanostructured catalysts for oxygen reduction reactions to fuel cell vehicles. *Nat. Nanotechnol.* **16**, 140–147 (2021).
6. J. Greeley, I. E. Stephens, A. S. Bondarenko, T. P. Johansson, H. A. Hansen, T. F. Jaramillo, J. Rossmeisl, I. Chorkendorff, J. K. Nørskov, Alloys of platinum and early transition metals as oxygen reduction electrocatalysts. *Nat. Chem.* **1**, 552–556 (2009).
7. W. Xia, A. Mahmood, Z. Liang, R. Zou, S. Guo, Earth-abundant nanomaterials for oxygen reduction. *Angew. Chem. Int. Ed. Engl.* **55**, 2650–2676 (2016).
8. J. K. Norskov, T. Bligaard, J. Rossmeisl, C. H. Christensen, Towards the computational design of solid catalysts. *Nat. Chem.* **1**, 37–46 (2009).
9. D. Wu, X. Shen, Y. Pan, L. Yao, Z. Peng, Platinum alloy catalysts for oxygen reduction reaction: Advances, challenges and perspectives. *ChemNanoMat* **6**, 32–41 (2020).
10. M. Liu, Z. Zhao, X. Duan, Y. Huang, Nanoscale structure design for high-performance Pt-based ORR catalysts. *Adv. Mater.* **31**, e1802234 (2019).
11. J. Fan, M. Chen, Z. Zhao, Z. Zhang, S. Ye, S. Xu, H. Wang, H. Li, Bridging the gap between highly active oxygen reduction reaction catalysts and effective catalyst layers for proton exchange membrane fuel cells. *Nat. Energy* **6**, 475–486 (2021).
12. I. E. L. Stephens, J. Rossmeisl, I. Chorkendorff, Toward sustainable fuel cells. *Science* **354**, 1378–1379 (2016).
13. L. Bu, J. Ding, S. Guo, X. Zhang, D. Su, X. Zhu, J. Yao, J. Guo, G. Lu, X. Huang, A general method for multimetallic platinum alloy nanowires as highly active and stable oxygen reduction catalysts. *Adv. Mater.* **27**, 7204–7212 (2015).
14. S. Chen, M. Li, M. Gao, J. Jin, M. A. van Spronsen, M. B. Salmeron, P. Yang, High-performance Pt-Co nanoframes for fuel-cell electrocatalysis. *Nano Lett.* **20**, 1974–1979 (2020).

15. C. Cui, L. Gan, H. H. Li, S. H. Yu, M. Heggen, P. Strasser, Octahedral PtNi nanoparticle catalysts: Exceptional oxygen reduction activity by tuning the alloy particle surface composition. *Nano Lett.* **12**, 5885–5889 (2012).
16. J. Wu, A. Gross, H. Yang, Shape and composition-controlled platinum alloy nanocrystals using carbon monoxide as reducing agent. *Nano Lett.* **11**, 798–802 (2011).
17. T. He, W. Wang, F. Shi, X. Yang, X. Li, J. Wu, Y. Yin, M. Jin, Mastering the surface strain of platinum catalysts for efficient electrocatalysis. *Nature* **598**, 76–81 (2021).
18. C. Cui, L. Gan, M. Heggen, S. Rudi, P. Strasser, Compositional segregation in shaped Pt alloy nanoparticles and their structural behaviour during electrocatalysis. *Nat. Mater.* **12**, 765–771 (2013).
19. R. Borup, J. Meyers, B. Pivovar, Y. S. Kim, R. Mukundan, N. Garland, D. Myers, M. Wilson, F. Garzon, D. Wood, P. Zelenay, K. More, K. Stroh, T. Zawodzinski, J. Boncella, J. E. McGrath, M. Inaba, K. Miyatake, M. Hori, K. Ota, Z. Ogumi, S. Miyata, A. Nishikata, Z. Siroma, Y. Uchimoto, K. Yasuda, K. I. Kimijima, N. Iwashita, Scientific aspects of polymer electrolyte fuel cell durability and degradation. *Chem. Rev.* **107**, 3904–3951 (2007).
20. J. P. Braaten, X. Xu, Y. Cai, A. Kongkanand, S. Litster, Contaminant cation effect on oxygen transport through the ionomers of polymer electrolyte membrane fuel cells. *J. Electrochem. Soc.* **166**, F1337–F1343 (2019).
21. H. Abe, F. Matsumoto, L. R. Alden, S. C. Warren, H. D. Abruña, F. J. DiSalvo, Electrocatalytic performance of fuel oxidation by Pt_3Ti nanoparticles. *J. Am. Chem. Soc.* **130**, 5452–5458 (2008).
22. Y. Yan, J. S. Du, K. D. Gilroy, D. Yang, Y. Xia, H. Zhang, Intermetallic nanocrystals: Syntheses and catalytic applications. *Adv. Mater.* **29**, 1605997 (2017).
23. E. Antolini, Alloy vs. intermetallic compounds: Effect of the ordering on the electrocatalytic activity for oxygen reduction and the stability of low temperature fuel cell catalysts. *Appl. Catal. Environ.* **217**, 201–213 (2017).
24. J. T. L. Gamler, H. M. Ashberry, S. E. Skrabalak, K. M. Koczkur, Random alloyed versus intermetallic nanoparticles: A comparison of electrocatalytic performance. *Adv. Mater.* **30**, e1801563 (2018).
25. H. Y. Kim, S. H. Joo, Recent advances in nanostructured intermetallic electrocatalysts for renewable energy conversion reactions. *J. Mater. Chem. A* **8**, 8195–8217 (2020).
26. Y. Ma, A. N. Kuhn, W. Gao, T. Al-Zoubi, H. Du, X. Pan, H. Yang, Strong electrostatic adsorption approach to the synthesis of sub-three nanometer intermetallic platinum–cobalt oxygen reduction catalysts. *Nano Energy* **79**, 105465 (2021).
27. C.-L. Yang, L.-N. Wang, P. Yin, J. Liu, M.-X. Chen, Q.-Q. Yan, Z.-S. Wang, S.-L. Xu, S.-Q. Chu, C. Cui, H. Ju, J. Zhu, Y. Lin, J. Shui, H.-W. Liang, Sulfur-anchoring synthesis of platinum intermetallic nanoparticle catalysts for fuel cells. *Science* **374**, 459–464 (2021).
28. Z. Qin, T. Wang, Z. Yao, Q. Li, Unconventional intermetallic noble metal nanocrystals for energy-conversion electrocatalysis. *EES Catal.* **2**, 545–555 (2024).
29. J. Guan, D. Dong, N. A. Khan, Y. Zheng, Emerging Pt-based intermetallic nanoparticles for the oxygen reduction reaction. *Chem. Commun.* **60**, 1811–1825 (2024).
30. F. Lin, M. Li, L. Zeng, M. Luo, S. Guo, Intermetallic nanocrystals for fuel-cells-based electrocatalysis. *Chem. Rev.* **123**, 12507–12593 (2023).
31. D. Y. Chung, S. W. Jun, G. Yoon, S. G. Kwon, D. Y. Shin, P. Seo, J. M. Yoo, H. Shin, Y. H. Chung, H. Kim, B. S. Mun, K. S. Lee, N. S. Lee, S. J. Yoo, D. H. Lim, K. Kang, Y. E. Sung, T. Hyeon, Highly durable and active PtFe nanocatalyst for electrochemical oxygen reduction reaction. *J. Am. Chem. Soc.* **137**, 15478–15485 (2015).
32. D. Wang, H. L. Xin, R. Hovden, H. Wang, Y. Yu, D. A. Muller, F. J. DiSalvo, H. D. Abruna, Structurally ordered intermetallic platinum-cobalt core-shell nanoparticles with enhanced activity and stability as oxygen reduction electrocatalysts. *Nat. Mater.* **12**, 81–87 (2013).
33. J. Liang, Y. Wan, H. Lv, X. Liu, F. Lv, S. Li, J. Xu, Z. Deng, J. Liu, S. Zhang, Y. Sun, M. Luo, G. Lu, J. Han, G. Wang, Y. Huang, S. Guo, Q. Li, H. Zhu, Metal bond strength regulation enables large-scale synthesis of intermetallic nanocrystals for practical fuel cells. *Nat. Mater.* **23**, 1259–1267 (2024).
34. H. Chen, D. Wang, Y. Yu, K. A. Newton, D. A. Muller, H. Abruna, F. J. DiSalvo, A surfactant-free strategy for synthesizing and processing intermetallic platinum-based nanoparticle catalysts. *J. Am. Chem. Soc.* **134**, 18453–18459 (2012).
35. D. C. L. Lee, F. V. Mikulec, J. M. Pelaez, B. Koo, B. A. Korgel, Synthesis and magnetic properties of silica-coated FePt nanocrystals. *J. Phys. Chem. B.* **110**, 11160–11166 (2006).
36. M. Chi, C. Wang, Y. Lei, G. Wang, D. Li, K. L. More, A. Lupini, L. F. Allard, N. M. Markovic, V. R. Stamenkovic, Surface faceting and elemental diffusion behaviour at atomic scale for alloy nanoparticles during in situ annealing. *Nat. Commun.* **6**, 8925 (2015).
37. H. Y. Kim, J. M. Kim, Y. Ha, J. Woo, A. Byun, T. J. Shin, K. H. Park, H. Y. Jeong, H. Kim, J. Y. Kim, S. H. Joo, Activity origin and multifunctionality of Pt-Based intermetallic nanostructures for efficient electrocatalysis. *ACS Catal.* **9**, 11242–11254 (2019).
38. Z. Yang, H. Yang, L. Shang, T. Zhang, Ordered PtFeIr intermetallic nanowires prepared through a silica-protection strategy for the oxygen reduction reaction. *Angew. Chem. Int. Ed. Engl.* **61**, e202113278 (2022).
39. J. Guo, L. Gao, X. Tan, Y. Yuan, J. Kim, Y. Wang, H. Wang, Y.-J. Zeng, S.-I. Choi, S. C. Smith, H. Huang, Template-directed rapid synthesis of Pd-based ultrathin porous intermetallic nanosheets for efficient oxygen reduction. *Angew. Chem. Int. Ed. Engl.* **60**, 10942–10949 (2021).
40. US Department of Energy (DOE), DOE Technical Targets for Polymer Electrolyte Membrane Fuel Cell Components (DOE, 2018).
41. Y. Ma, W. Gao, H. Shan, W. Chen, W. Shang, P. Tao, C. Song, C. Addiego, T. Deng, X. Pan, J. Wu, Platinum-based nanowires as active catalysts toward oxygen reduction reaction: In situ observation of surface-diffusion-assisted, solid-state oriented attachment. *Adv. Mater.* **29**, 1703460 (2017).
42. H.-Y. Chao, K. Venkatraman, S. Moniri, Y. Jiang, X. Tang, S. Dai, W. Gao, J. Miao, M. Chi, In situ and emerging transmission electron microscopy for catalysis research. *Chem. Rev.* **123**, 8347–8394 (2023).
43. W. Gao, P. Tieu, C. Addiego, Y. Ma, J. Wu, X. Pan, Probing the dynamics of nanoparticle formation from a precursor at atomic resolution. *Sci. Adv.* **5**, eaau9590 (2019).
44. J. G. Smith, K. J. Sawant, Z. Zeng, T. B. Eldred, J. Wu, J. P. Greeley, W. Gao, Disproportionation chemistry in K_2PtCl_4 visualized at atomic resolution using scanning transmission electron microscopy. *Sci. Adv.* **10**, eadi0175 (2024).
45. W. Qi, Y. Li, S. Xiong, S. T. Lee, Modeling size and shape effects on the order-disorder phase-transition temperature of CoPt nanoparticles. *Small* **6**, 1996–1999 (2010).
46. D. Alloyeau, C. Ricolleau, C. Mottet, T. Oikawa, C. Langlois, Y. Le Bouar, N. Braidy, A. Loiseau, Size and shape effects on the order-disorder phase transition in CoPt nanoparticles. *Nat. Mater.* **8**, 940–946 (2009).
47. G. Treglia, B. Legrand, F. Ducastelle, Segregation and ordering at surfaces of transition metal alloys: The tight-binding ising model. *Europhys. Lett.* **7**, 575–580 (1988).
48. B. Rellinghaus, E. Mohn, L. Schultz, T. Gemming, M. Acet, A. Kowalik, B. F. Kock, On the $L1_0$ ordering kinetics in Fe-Pt nanoparticles. *IEEE Trans. Magn.* **42**, 3048–3050 (2006).
49. D. Alloyeau, C. Langlois, C. Ricolleau, Y. Le Bouar, A. Loiseau, A TEM in situ experiment as a guideline for the synthesis of as-grown ordered CoPt nanoparticles. *Nanotechnology* **18**, 375301 (2007).
50. S. Muller, Bulk and surface ordering phenomena in binary metal alloys. *J. Phys. Condens. Matter* **15**, 1429–1500 (2003).
51. E. G. McRAE, T. M. Buck, Surface compositional ordering and domain walls in Cu_3Au. *Surf. Sci.* **227**, 67–72 (1990).
52. M. A. Vasiliev, Surface effects of ordering in binary alloys. *J. Phys. D Appl. Phys.* **30**, 3037–3070 (1997).
53. A. V. Ruban, H. L. Skriver, J. K. Nørskov, Surface segregation energies in transition-metal alloys. *Phys. Rev. B* **59**, 15990–16000 (1999).
54. M. Luo, Y. Sun, X. Zhang, Y. Qin, M. Li, Y. Li, C. Li, Y. Yang, L. Wang, P. Gao, G. Lu, S. Guo, Stable high-index faceted Pt skin on zigzag-like PtFe nanowires enhances oxygen reduction catalysis. *Adv. Mater.* **30**, 1705515 (2018).
55. H. Duan, Q. Hao, C. Xu, Nanoporous PtFe alloys as highly active and durable electrocatalysts for oxygen reduction reaction. *J. Power Sources* **269**, 589–596 (2014).
56. J. Li, Z. Xi, Y. T. Pan, J. S. Spendelow, P. N. Duchesne, D. Su, Q. Li, C. Yu, Z. Yin, B. Shen, Y. S. Kim, P. Zhang, S. Sun, Fe stabilization by intermetallic $L1_0$-FePt and Pt catalysis enhancement in $L1_0$-FePt/Pt nanoparticles for efficient oxygen reduction reaction in fuel cells. *J. Am. Chem. Soc.* **140**, 2926–2932 (2018).
57. Q. Li, L. Wu, G. Wu, D. Su, H. Lv, S. Zhang, W. Zhu, A. Casimir, H. Zhu, A. Mendoza-Garcia, S. Sun, New approach to fully ordered fct-FePt nanoparticles for much enhanced electrocatalysis in acid. *Nano Lett.* **15**, 2468–2473 (2015).
58. A. Jain, S. P. Ong, G. Hautier, W. Chen, W. D. Richards, S. Dacek, S. Cholia, D. Gunter, D. Skinner, G. Ceder, K. A. Persson, The Materials Project: A materials genome approach to accelerating materials innovation. *APL Mater.* **1**, 011002 (2013).
59. V. Stamenkovic, B. S. Mun, K. J. J. Mayrhofer, P. N. Ross, N. M. Markovic, J. Rossmeisl, J. Greeley, J. K. Nørskov, Changing the activity of electrocatalysts for oxygen reduction by tuning the surface electronic structure. *Angew. Chem. Int. Ed. Engl.* **118**, 2963–2967 (2006).
60. J. K. Nørskov, J. Rossmeisl, A. Logadottir, L. Lindqvist, J. R. Kitchin, T. Bligaard, H. Jónsson, Origin of the overpotential for oxygen reduction at a fuel-cell cathode. *J. Phys. Chem. B* **108**, 17886–17892 (2004).
61. G. Kresse, J. Furthmüller, Efficient iterative schemes for ab initio total-energy calculations using a plane-wave basis set. *Phys. Rev. B* **54**, 11169–11186 (1996).
62. G. Kresse, J. Hafner, Ab initio molecular dynamics for liquid metals. *Phys. Rev. B* **47**, 558–561 (1993).
63. G. Kresse, J. Hafner, Norm-conserving and ultrasoft pseudopotentials for first-row and transition elements. *J. Phys. Condens. Matter* **6**, 8245–8257 (1994).
64. P. E. Blöchl, O. Jepsen, O. K. Andersen, Improved tetrahedron method for Brillouin-zone integrations. *Phys. Rev. B* **49**, 16223–16233 (1994).
65. P. E. Blöchl, Projector augmented-wave method. *Phys. Rev. B* **50**, 17953–17979 (1994).
66. Y. He, Y. L. Wu, X. X. Zhu, J. N. Wang, Remarkable improvement of the catalytic performance of PtFe nanoparticles by structural ordering and doping. *ACS Appl. Mater. Interfaces* **11**, 11527–11536 (2019).
67. X. X. Du, Y. He, X. X. Wang, J. N. Wang, Fine-grained and fully ordered intermetallic PtFe catalysts with largely enhanced catalytic activity and durability. *Energy Environ. Sci.* **9**, 2623–2632 (2016).

68. Z. Yan, M. Wang, J. Liu, R. Liu, J. Zhao, Glycerol-stabilized $NaBH_4$ reduction at room-temperature for the synthesis of a carbon-supported Pt_xFe alloy with superior oxygen reduction activity for a microbial fuel cell. *Electrochim. Acta* **141**, 331–339 (2014).
69. J. Lee, J. M. Yoo, Y. Ye, Y. Mun, S. Lee, O.-H. Kim, H.-W. Rhee, H. I. Lee, Y.-E. Sung, J. Lee, Development of highly stable and mass transfer-enhanced cathode catalysts: Support-free electrospun intermetallic FePt nanotubes for polymer electrolyte membrane fuel cells. *Adv. Energy Mater.* **5**, 1402093 (2015).
70. L. Chong, J. Wen, J. Kubal, F. G. Sen, J. Zou, J. Greeley, M. Chan, H. Barkholtz, W. Ding, D.-J. Liu, Ultralow-loading platinum-cobalt fuel cell catalysts derived from imidazolate frameworks. *Science* **362**, 1276–1281 (2018).
71. W. S. Jung, B. N. Popov, New method to synthesize highly active and durable chemically ordered fct-PtCo cathode catalyst for PEMFCs. *ACS Appl. Mater. Interfaces* **9**, 23679–23686 (2017).
72. M. Gummalla, S. C. Ball, D. A. Condit, S. Rasouli, K. Yu, P. J. Ferreira, D. J. Myers, Z. Yang, Effect of particle size and operating conditions on Pt_3Co PEMFC cathode catalyst durability. *Catalysts* **5**, 926–948 (2015).
73. Z. Qiao, C. Wang, C. Li, Y. Zeng, S. Hwang, B. Li, S. Karakalos, J. Park, A. J. Kropf, E. C. Wegener, Q. Gong, H. Xu, G. Wang, D. J. Myers, J. Xie, J. S. Spendelow, G. Wu, Atomically dispersed single iron sites for promoting Pt and Pt_3Co fuel cell catalysts: Performance and durability improvements. *Energy Environ. Sci.* **14**, 4948–4960 (2021).
74. F. Godínez-Salomón, R. Mendoza-Cruz, M. J. Arellano-Jimenez, M. Jose-Yacaman, C. P. Rhodes, Metallic two-dimensional nanoframes: Unsupported hierarchical nickel–platinum alloy nanoarchitectures with enhanced electrochemical oxygen reduction activity and stability. *ACS Appl. Mater. Interfaces* **9**, 18660–18674 (2017).
75. X. Peng, S. Zhao, T. J. Omasta, J. M. Roller, W. E. Mustain, Activity and durability of Pt-Ni nanocage electocatalysts in proton exchange membrane fuel cells. *Appl. Catal. Environ.* **203**, 927–935 (2017).
76. R. Sakamoto, K. Omichi, T. Furuta, M. Ichikawa, Effect of high oxygen reduction reaction activity of octahedral PtNi nanoparticle electrocatalysts on proton exchange membrane fuel cell performance. *J. Power Sources* **269**, 117–123 (2014).
77. B. Han, C. E. Carlton, A. Kongkanand, R. S. Kukreja, B. R. Theobald, L. Gan, R. O'Malley, P. Strasser, F. T. Wagner, Y. Shao-Horn, Record activity and stability of dealloyed bimetallic catalysts for proton exchange membrane fuel cells. *Energy Environ. Sci.* **8**, 258–266 (2015).
78. G. Wang, B. Huang, L. Xiao, Z. Ren, H. Chen, D. Wang, H. D. Abruña, J. Lu, L. Zhuang, Pt skin on AuCu intermetallic substrate: A strategy to maximize Pt utilization for fuel cells. *J. Am. Chem. Soc.* **136**, 9643–9649 (2014).
79. N. Cheng, L. Zhang, S. Mi, H. Jiang, Y. Hu, H. Jiang, C. Li, $L1_2$ atomic ordered substrate enhanced Pt-skin Cu_3Pt catalyst for efficient oxygen reduction reaction. *ACS Appl. Mater. Interfaces* **10**, 38015–38023 (2018).
80. A. Kongkanand, N. P. Subramanian, Y. Yu, Z. Liu, H. Igarashi, D. A. Muller, Achieving high-power PEM fuel cell performance with an ultralow-Pt-content core–shell catalyst. *ACS Catal.* **6**, 1578–1583 (2016).
81. T.-W. Song, M.-X. Chen, P. Yin, L. Tong, M. Zuo, S.-Q. Chu, P. Chen, H.-W. Liang, Intermetallic PtFe electrocatalysts for the oxygen reduction reaction: Ordering degree-dependent performance. *Small* **18**, e2202916 (2022).

Acknowledgments

Funding: This work was supported by the National Science Foundation of China 21875137 to J.W., National Science Foundation of China 51521004 to J.W., National Science Foundation of China 51420105009 to J.W., National Science Foundation of China 23Z990201030 to W.G., Program of Shanghai Academic/Technology Research Leader project no. 23XD1422100 to J.W., Innovation Program of Shanghai Municipal Education Commission project no. 2019-01-07-00-02-E00069 to T.D. and J.W., The 111 Project no. B16032 to J.W., and Center of Hydrogen Science and Joint Research Center for Clean Energy Materials at Shanghai Jiao Tong University to J.W.

Author contributions: Conceptualization: J.W., W.G., X.P., and W.C. Methodology: Y.M., W.G., P. Tao, F.L., J.X., H.Z., X.P., and J.W. Investigation: Y.M., W.G., P. Tieu, L.P., J.W., J.P., J.T., F.L., and P.T. Visualization: Y.M., W.G., C.S., J.W., J.P., J.T., P. Tao, and T.D. Funding acquisition: J.W., X.P., and D.T. Project administration: J.W., X.P., and Y.M. Supervision: J.W., X.P., Y.M., and T.D. Data curation: Y.M., W.G., J.W., J.P., and T.D. Validation: Y.M., W.G., J.W., X.P., J.P., J.T., P. Tao, J.X., and H.Z. Formal analysis: Y.M., W.G., J.W., J.P., J.T., J.X., and H.Z. Writing—original draft: Y.M., W.G., W.C., and H.Z. Writing—review and editing: Y.M., W.G., J.P., J.T., J.X., H.H., W.C., L.P., W.S., C.S., H.Z., X.P., T.D., and J.W. **Competing interests:** The authors declare that they have no competing interests. **Data and materials availability:** All data needed to evaluate the conclusions in the paper are present in the paper and/or the Supplementary Materials.

Submitted 17 February 2024
Accepted 13 September 2024
Published 18 October 2024
10.1126/sciadv.ado4935